

Journal of Materials Chemistry A

Accepted Manuscript



This is an *Accepted Manuscript*, which has been through the Royal Society of Chemistry peer review process and has been accepted for publication.

Accepted Manuscripts are published online shortly after acceptance, before technical editing, formatting and proof reading. Using this free service, authors can make their results available to the community, in citable form, before we publish the edited article. We will replace this *Accepted Manuscript* with the edited and formatted *Advance Article* as soon as it is available.

You can find more information about *Accepted Manuscripts* in the [Information for Authors](#).

Please note that technical editing may introduce minor changes to the text and/or graphics, which may alter content. The journal's standard [Terms & Conditions](#) and the [Ethical guidelines](#) still apply. In no event shall the Royal Society of Chemistry be held responsible for any errors or omissions in this *Accepted Manuscript* or any consequences arising from the use of any information it contains.

Super-Ion Inspired Colorful Hybrid Perovskite Solar Cells

*Hong Fang, Puru Jena**

Department of Physics, Virginia Commonwealth University, 701 West Grace Street, 23284, VA, United States
E-mail: pjena@vcu.edu

Abstract

Clean and sustainable energy is one of the greatest challenges of this century. Of the several renewable energy sources that can address this challenge, nothing has greater potential than solar energy. However, to harness the solar power and to ensure its world-wide uptake, efficient, cheap, environmentally benign, and durable solar cells are essential. The unprecedented enhancement in the power conversion efficiency of hybrid perovskite solar cells from 3.9 % in 2009 to over 20 % today shows their great promise to meet the above challenges, provided issues with their stability and environmental impact can be addressed. Despite considerable research in the past five years, answers to some fundamental questions as well as an atomic level understanding of these materials remain a challenge. Using multi-scale approach and a comprehensive study of over 40 materials, we have identified the key parameters and mechanisms that control the basic properties and the stability of hybrid perovskites. We show that these materials can be viewed as super alkali halide crystals where alkali and halogen ions are respectively replaced by super-alkali and super-halogen species. This opens the path to a new series of hybrid perovskites based on super-ions as building blocks with improved stability and functionality.

1. Introduction

Hybrid perovskites with the formula AMX_3 (A = organic cation; M = metal; X = halogen) have emerged as a new generation of photovoltaic cells. Due to their high conversion efficiency, excellent light-emission properties, easy solution-based synthesis, and tunable optical band gaps from visible to infrared regions, these materials are considered to be “the next big thing” in solar cells^[1-11] and other optoelectronic devices^[12-14]. However, several important issues such as fundamental understanding of the relationship between the photoexcitation properties and chemical structures of hybrid perovskites, their durability under working conditions, as well as the synthesis of their environment-friendly (lead-free) analogues remain a challenge^[5, 10]. Using a comprehensive multi-scale approach based on the available experimental data, density functional theory and molecular dynamics simulations we address these challenges and provide an atomic-level understanding of the structure-property relationships of a large number of organic-inorganic hybrid perovskites. The study allows us to answer the fundamental questions such as: what are the driving factors that control the band gaps of hybrid perovskites and how are they related to their underlying chemical structure? What is the degradation mechanism of these materials under moisture? Can such an understanding allow us to design and synthesize new hybrid perovskites with improved properties? Finding answers to the above questions is made possible by introducing a new vision of these materials – we view them as super alkali halide crystals where the alkali cations and halogen anions are replaced by super-ions that mimic their respective properties. We show that this new understanding can be used to guide experiments in the design and synthesis of a new generation of lead-free hybrid perovskites with possible improvement in their stability and physico-chemical properties.

Simply by looking at the chemical formula of the hybrid perovskites (AMX_3 , A = CH_3NH_3 , $HC(NH_2)_2$; M = Ge, Sn, Pb; X = Cl, Br, I), it is tempting to see them as ionic crystals like the alkali halides, except that, instead of the alkalis ($Li^+ \sim Cs^+$) and the halogens

($\text{Cl}^- \sim \text{I}^-$), these materials are composed of super ions that are atomic clusters with their own structures. Ever since these materials and their inorganic analogues with $A = \text{alkali (Rb, Cs)}$ were synthesized 20-30 years ago, it was noted that the deformation of the MX_6 octahedron results in isolated $[\text{MX}_3]^-$ pyramids^[15, 16-17, 19]. Analysis of the electronic band structures of $\text{CH}_3\text{NH}_3\text{PbX}_3$ suggests that the main interaction between $[\text{CH}_3\text{NH}_3]^+$ and $[\text{PbX}_3]^-$ is ionic^[20]. The large value of the dielectric constant and the frequency-dependent behavior of its imaginary part measured in $\text{CH}_3\text{NH}_3\text{PbI}_3$ indicate the ionic character of the crystal^[21].

The A^+ and $[\text{MX}_3]^-$ super-ions with positive and negative charge have been known in the literature for some time as “super-alkalis”^[22] and “super-halogens”, respectively^[23]. Super-alkalis (super-halogens) are composed of two or more elements and contain one extra electron (one less electron) than that needed for electronic shell closure. Thus, the former behave like alkali atoms while the latter behave like halogen atoms. Because the extra charge in these super-ions is distributed over a larger phase space than that in alkali or halogen ions, the energy to remove an electron from a super-alkali (i.e. the ionization potential, IP) and the energy gained in adding an electron to a neutral super-halogen moiety (i.e. electron affinity, EA) are different from those of their atomic counterparts. Indeed, the IP of super-alkalis are *less* than those of alkali atoms while the EA of super-halogens are *larger* than those of halogen atoms. Thus, hybrid perovskites can be classified as super-salts^[24] composed of A^+ and $[\text{MX}_3]^-$ ions just as normal salts are composed of alkali cations and halogen anions. By replacing halogen X in MX_3 by a super-halogen moiety, another highly electronegative species called hyper-halogens^[25] can be created that also mimic the chemistry of halogens. A recent example of such a species is $[\text{Al}(\text{BH}_4)_4]^-$, created by replacing halogen atom X in $[\text{AlX}_4]^-$ by BH_4 super-halogens. The BH_4 moiety mimics the chemistry of halogens. Its vertical detachment energy, i.e. energy needed to remove the electron from the anion without changing its geometry, namely 4.4 eV, is larger than that of any halogen, leading to the

synthesis of a hyper-salt, $\text{KAl}(\text{BH}_4)_4$ [26-27]. This synthesis makes us wonder if a new class of hybrid perovskite (AMX_3) solar cells can also be created by replacing halogens, X with BH_4 . Considerable research over the past 30 years has revealed a large number of super-alkali, super-halogen, and hyper-halogen moieties. Our premise is that this knowledge can be used in the design of new hybrid perovskites.

To establish that A^+ and $[\text{MX}_3]^-$ moieties are indeed super-alkalis and super-halogens, respectively, we optimized their structures using density functional theory and calculated their corresponding IPs and EAs. These results, given in the Table S1 of the Supporting Information [28], confirm that these moieties are super-alkalis and super-halogens and thus hybrid perovskites can be regarded as super-salts.

It has been known for a long time that there exists a close relationship between the ionic radius and bond ionicity of ionic crystals with their band gaps [29-30]. With the hybrid perovskites seen as super alkali halides made of super ions, it is essential to find the implications of their ionic character on their bulk properties, especially those relevant to the photovoltaic applications. From alkali halides, it is well-known that the ionic crystals have large band gaps. The narrowest band gap among the series is 6.0 eV of KI [28] -- much higher than the visible range (1.5~3.3 eV) needed for solar cells. So, the first question is how hybrid perovskites as ionic crystals could have such narrow band gaps within the visible spectrum? Owing to the ionic binding, alkali halides possess some distinctive features in their crystal structures. Do the hybrid perovskites show similar features and if so how the structure of super ions may modify them?

2. Result and Discussion

2.1. A Physical Model for Hybrid Perovskites

Bearing these questions in mind, we developed a model to identify the key parameters that determine the band gaps of alkali halide crystals – these are the effective ionic radii of the composite ions and the bonding ionicity. Detailed derivation and discussion of the model are given in the Supporting Information Sec. II ^[28]. According to the model, higher bonding ionicity, defined as the electronegativity difference between the anion and the cation (Supporting Information Equation S1-S3), can result in larger band gap. For a certain cation, the band gap will decrease with larger ionic radius R_- of the anion. The material with larger lattice size L per molecular unit tends to show smaller band gap. These trends obtained from our model are consistent with the empirical Fajans' rules ^[31] and the early finding of the hetero-polar (ionic) part of the energy gap of semiconductors ^[29]. The position of the band gap (in other words, the energy of the maximum of the valence band) will move upwards in energy with the decrease of the bonding ionicity (as discussed in Supporting Information Sec. III).

Proper band gaps as well as the arrangement of the energy bands between the hybrid perovskites and the electron/hole harvesting materials are essential to make solar cells with high efficiency ^[6, 11, 32-33]. Our model allows us to explain the available experimental results on the band gaps of hybrid perovskites by simply comparing the values of their bonding ionicity ($\Delta\chi$ in Supporting Sec. II) from cluster calculations. Experiments show that $\text{CH}_3\text{NH}_3(\text{Sn}/\text{Pb})\text{I}_3$ has smaller band gap and higher top of the valence band ^[6, 11] than $\text{CH}_3\text{NH}_3(\text{Sn}/\text{Pb})\text{Br}_3$. Similarly, $\text{CH}_3\text{NH}_3\text{SnI}_3$ has smaller band gap and higher top of the valence band than $\text{CH}_3\text{NH}_3\text{PbI}_3$ [32]. Indeed, if we compare the ionicity ($\Delta\chi$) of the $\text{A}^+--[\text{MX}_3]^-$ bonds as listed in Supporting Table S2 ^[28], the trend is that, with the same cation, the ionicity increases down the group from $\text{M} = \text{Ge}, \text{Sn}, \text{Pb}$ while it decreases down the group from $\text{X} = \text{Cl}, \text{Br}, \text{I}$. Specifically, we see that $[\text{CH}_3\text{NH}_3]^+--[(\text{Sn}/\text{Pb})\text{I}_3]^-$ has smaller ionicity than $[\text{CH}_3\text{NH}_3]^+--[(\text{Sn}/\text{Pb})\text{Br}_3]^-$ and $[\text{CH}_3\text{NH}_3]^+--[\text{SnI}_3]^-$ has smaller ionicity compared to

$[\text{CH}_3\text{NH}_3]^+--[\text{PbI}_3]^-$. The elementary alkali halides A^+B^- show the same trend, i.e. with the same cation A (= group 1), the ionicity decreases down the group of B (= Cl, Br, I).

2.2. Effective Ionic Radii of the Super-Ions

As seen from the Pauling's rules^[34] in the study of alkali halides, the effective ionic radii of the composite ions are akin to their basic chemical and physical properties. Similarly, as indicated by our model, knowing the radii of the super-ions is helpful in the analysis of band gaps and structural stability of the hybrid perovskites as super alkali halide crystals.

Unlike the elementary ions, the super-alkalis and super-halogens are themselves atomic clusters, hence they have their own geometries with internal degrees of freedom. Therefore, the first step in computing the ionic radii is to determine the individual geometries of the cations and anions in hybrid perovskites. To achieve this goal, we collected the available experimental data^[11, 17-18, 19, 35-37] on the structures of $(\text{Cs/Rb})(\text{Ge/Sn})(\text{Cl/Br/I})_3$, $\text{CH}_3\text{NH}_3(\text{Ge/Sn})\text{Cl}_3$, $\text{CH}_3\text{NH}_3\text{Sn}(\text{Br/I})_3$ and $\text{HC}(\text{NH}_2)_2\text{SnI}_3$. For the hybrid perovskites where no experimental data are available, such as $\text{CH}_3\text{NH}_3\text{Ge}(\text{Br/I})_3$, $\text{HC}(\text{NH}_2)_2\text{Ge}(\text{Cl/Br/I})_3$, $\text{HC}(\text{NH}_2)_2\text{Sn}(\text{Cl/Br})_3$, $\text{CH}_3\text{NH}_3(\text{Ge/Sn})(\text{BH}_4)_3$ and $\text{HC}(\text{NH}_2)_2(\text{Ge/Sn})(\text{BH}_4)_3$, we carried out *ab initio* molecular dynamics simulations to find their structures under ambient conditions, as shown in Supporting Information Sec. IV and V^[28]. These data as well as the geometries of their cluster analogues are presented in Supporting Table S3 and S4^[28]. Note that we exclude the data on hybrid perovskites containing Pb as the focus of this study is on the lead-free materials. However, the conclusions should also apply to the lead-based series.

It is found from both experiments^[15-20] and our calculations that the structures of organic super-alkalis remain almost constant in all materials and hardly change from their geometry in the gas phase. Similarly, there is little change in the geometry of the same super-halogen $[\text{MX}_3]^-$ in different materials. A typical relative difference in both the bond distance and bond

angle data is less than 5%, even when compared to the isolated clusters. However, the agreement between structures of hyper-halogens $[\text{Ge}(\text{BH}_4)_3]^-$ and $[\text{Sn}(\text{BH}_4)_3]^-$ in crystals and isolated clusters is somewhat worse, with X-X distances and M-X-X angles differing by 7% and 18%, respectively. This may be due to the repulsion between the hydrogen atoms in the neighboring $[\text{BH}_4]^-$ clusters^[38], causing the hyper-halogens acquire a more compact geometry (shorter X-X distance and bigger M-X-X angle) in a restrictive crystal environment.

Besides evaluating the structures of super-halogens in various materials under ambient conditions, we should also consider the structural change of the super-ions in different phases of a given material. It is noted that the studied hybrid perovskites tend to adopt the cubic phase at high temperatures (as shown in the last row of Supporting Table S3). The super-ions $[\text{MX}_3]^-$ in such high symmetric phase will appear to be regular octahedral. The halogen atom X on the vertices of an octahedron is shared by two neighboring super-halogens, i.e. each X provides ‘half’ electron to bond with the center metal ion to make $[(\text{M}^{+1/2})_2(\text{X}^{-1/2})_6]^- = [\text{MX}_3]^-$. We found that, although the geometry of the super-halogen in a crystal changes with different phases of the material, its geometrical dimension is still bounded by a characteristic triangle defined by the basic bonding properties of the isolated atomic cluster. These are discussed in details in Supporting Sec.VI^[28].

Based on the discussions above, we defined the effective ionic radii for super-alkalis and super-halogens by using the experimental and calculated interionic distances and dielectric constants. The first strategy we adopt is to find a set of radii that best fit to these data directly and that are comparable with Shannon’s radii^[39] of the elementary ions. The second strategy is to compute a set of radii by utilizing the interionic distance data in a lattice-energy model of an ionic crystal. These radii are defined along the lines of Pauling’s radii^[40] of the elementary alkalis and halides. Details of the methods are given in Supporting Sec.VI^[28]. The calculated radii of the super-ions are listed in Supporting Table S5-S7 for the Shannon-type and Table

S8-S9 for the Pauling-type. Radii of the super-halogens for their asymmetric form (pyramidal) are also defined and given in Supporting Table S11.

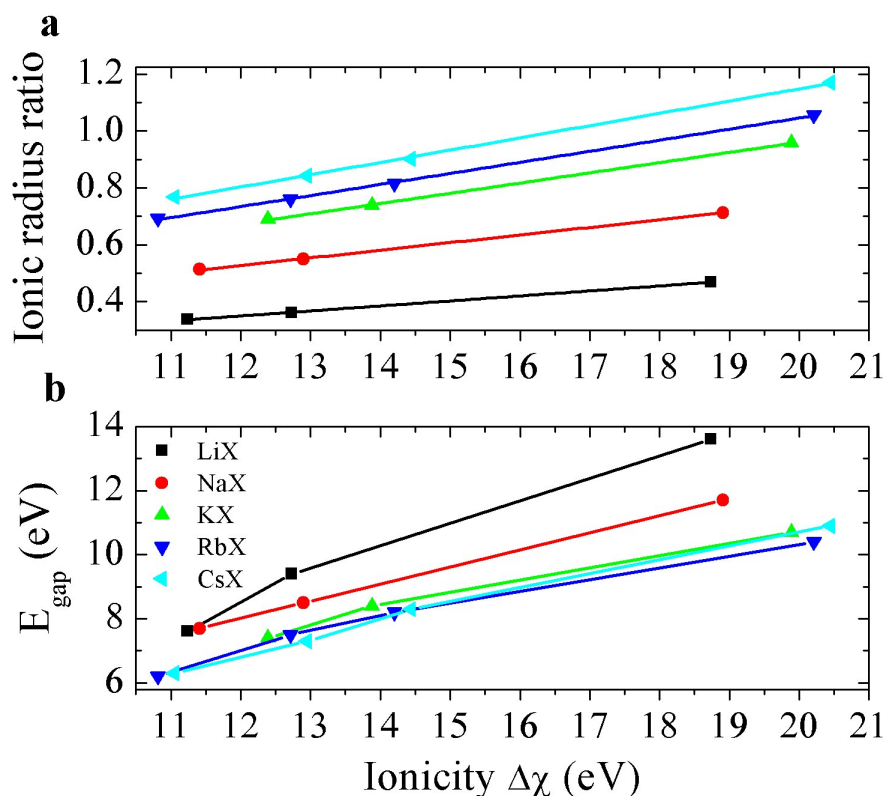


Figure 1. Ionic radius ratio and the band gaps of alkali halides against the bond ionicity. (a) Cation vs. anion radii ratio, R_+/R_- calculated using the Pauling radii^[28] against the ionicity for the alkali halides. We found similar results using the Shannon-type radii. (b) Band gaps of alkali halide crystals obtained from experiments against the calculated ionicity. For LiX, NaX and KX, the data points on each curve correspond to X = F, Cl, Br from right to left, while for RbX and CsX, additional data points of X = I are also included to the left. All these data can be found in Supporting Table S12^[28].

With the effective ionic radii of the super-ions properly defined, we can compute the radius ratio of the cation vs. anion and compare them to the elementary alkali halides. The material with large radius ratio is likely to show higher ionicity $\Delta\chi$, given that it becomes easier to remove an electron as the cation gets larger while it is easier for a smaller anion to hold the added electron. Such behavior is indeed found for the ordinary alkali halides, as shown in Figure 1a. Given the almost linear relation between the radius ratio and the ionicity,

there is a good correlation between the ionicity and the band gaps of alkali halide crystals as shown in Figure 1b. For the super alkali halides, however, there are two ways to increase the bond ionicity -- one is to increase the radius ratio by reducing the size of the super halogens $[\text{MX}_3]^-$ using smaller halogen "X" and the other is to use a more metallic "M", e.g. Sn compared to Ge. In the latter way, the radius ratio actually decreases with increasing ionicity as shown in Figure 2a (by comparing the data of $\text{A}[\text{SnX}_3]$ and $\text{A}[\text{GeX}_3]$ for the same A and X). We will further elaborate this point later when we introduce the use of hyper halogens (Supporting Sec. I^[28]). Comparing Figure 1 and Figure 2, we can see that, with the super-ions, one can achieve lower ionicity and lower radius ratio than the ordinary ions in the periodic table, hence much smaller band gaps for the super alkali halide crystals. To find an alkali that has larger radius and smaller electron negativity than Cs, one has to go further down the group 1 element. However, Fr (Francium) is highly radioactive and unstable. In fact, the element shows higher electronegativity than Cs due to the relativistic effect^[41]. Similarly, going further down the group 7 elements beyond iodine, At (Astatine) suffers from the same drawback as Fr. Here, we find that the stable non-radioactive super-alkali can have smaller electronegativity and larger radius than Cs and the super-halogens $[\text{MX}_3]^-$ can have larger radius and smaller electronegativity than iodine (see Supporting Table S2^[28]).

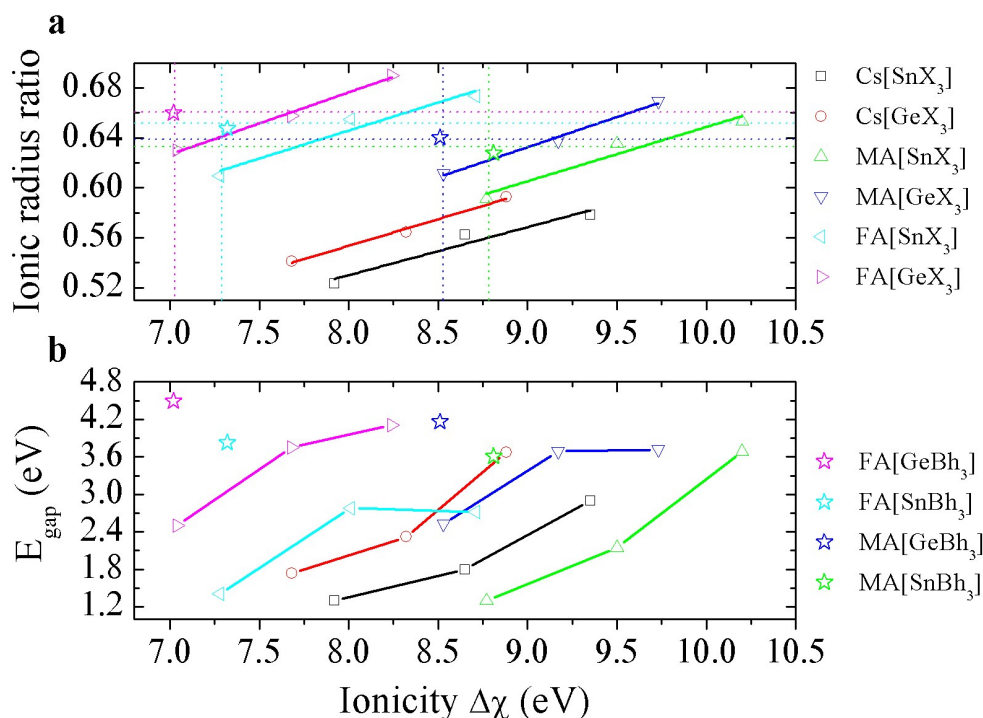


Figure 2. Ionic radius ratio and the band gaps of hybrid perovskites against the bond ionicity. (a) Cation vs. anion radii ratio, R_+/R_- for the hybrid perovskites composed of super- and hyper-halogens (Supporting Sec. I^[28]). MA and FA stand for CH_3NH_3 and $\text{HC}(\text{NH}_2)_2$, respectively. (b) The band gaps of hybrid perovskites obtained either from experiments or our calculations using HSE (see Supporting Sec. VIII for band structures and Sec. IX for electronic DoS^[28]) functional against ionicity. In each case with super-halogens, the data points correspond to $X = \text{Cl}, \text{Br}, \text{I}$ from right to left. “Bh” stands for (BH_4) . For CsSnCl_3 , we used the band gap of its cubic phase stabilized around 350 K. Its low-temperature monoclinic phase shows a value of 4.5 eV. All the data can be found in the Supporting Table S13^[28]. The dotted lines show that the hyper-salts show almost identical ionicity and radius ratio with their super-salt counterparts with $X = \text{I}$ and Br , respectively.

We have introduced a new class of hybrid perovskites $\text{A}[\text{MX}_3]$ where the $[\text{MX}_3]^-$ super-halogens are replaced by hyper-halogens^[42], $[\text{M}(\text{BH}_4)_3]^-$, as mentioned in Supporting Sec. I. Besides using the molecular dynamics simulations to study the stability of these crystalline hybrid perovskites composed of hyper-halogens (Supporting Sec. IV^[28]), we also carried out lattice dynamics calculations for $\text{CH}_3\text{NH}_3\text{Ge}(\text{BH}_4)_3$ and $\text{CH}_3\text{NH}_3\text{Sn}(\text{BH}_4)_3$ based on pseudo-cubic unit cells obtained from the molecular simulation under ambient conditions (Supporting Sec. X^[28]). The results are shown in Supporting Figure S14^[28]. The discontinuities appearing in the phonon dispersions at the center of the Brillouin zone (Γ point) are caused by the splitting of the longitudinal and transverse optic modes approaching the Γ -point. Such feature

is commonly found in ionic crystals with non-cubic symmetry due to the polarized vibrations of the longitudinal modes ^[43]. At this point, we also want to draw readers' attention to the recent experimental work where more than 30 new perovskite materials have been successfully prepared by replacing halogens with $[\text{BH}_4]^-$ ^[38].

Unlike the alkali halides whose ionicity increases with larger ionic radius ratio (Figure 1a), the trend is opposite when the $[\text{M}(\text{BH}_4)_3]^-$ hyper-halogens are bound to the same super-alkali. As shown in Figure 2a, for $\text{HC}(\text{NH}_2)_2[\text{Ge}(\text{BH}_4)_3]$ vs. $\text{HC}(\text{NH}_2)_2[\text{Sn}(\text{BH}_4)_3]$ and $[\text{CH}_3\text{NH}_3][\text{Ge}(\text{BH}_4)_3]$ vs. $[\text{CH}_3\text{NH}_3][\text{Sn}(\text{BH}_4)_3]$, the ionicity decreases as the radius ratio increases. This can be explained by referring to the natural bond orbital analysis (NBO) of the corresponding super-ions, as shown in the Supporting Sec. VII ^[28]. Although $[\text{Sn}(\text{BH}_4)_3]^-$ has larger ionic radius than $[\text{Ge}(\text{BH}_4)_3]^-$, the more positive charge on the Sn metal ion compared to Ge is likely to capture the electron more strongly, as suggested by the higher charge states of B and H in $[\text{Sn}(\text{BH}_4)_3]^-$. Previously, we have seen such behavior for the super-halogens $[\text{MX}_3]^-$, where we find that one can replace Ge with Sn to increase the bond ionicity with reduced radius ratio. The behavior already shows how the internal degrees of freedom (either structural or chemical) of the super-ions can make a difference compared to the elementary ions.

2.3. Band Gaps of Hybrid Perovskites

We now compare the band gaps of (super) alkali halide crystals calculated from our simple model with those available from experiments or our calculations (Supporting Sec. VIII and IX) using the HSE functional (see Computational Methods) in Figure 3. Note that our model based on simple ionic bonding in a one-dimensional lattice produces qualitatively, if not quantitatively, correct behavior of the band gaps of the studied materials. All these data are given in Supporting Table S13 ^[28]. It shows that the band gap of the hybrid perovskites are

indeed a function of the basic properties of ionicity and ionic radii as implemented in our model. The small band gaps of the hybrid perovskites (as super alkali halides) shown in Figure 3b compared to the alkali halides as shown in Figure 3a are due to the size effect of their composite ions – these are super-ions having larger sizes compared to the ordinary alkali and halogen ions.

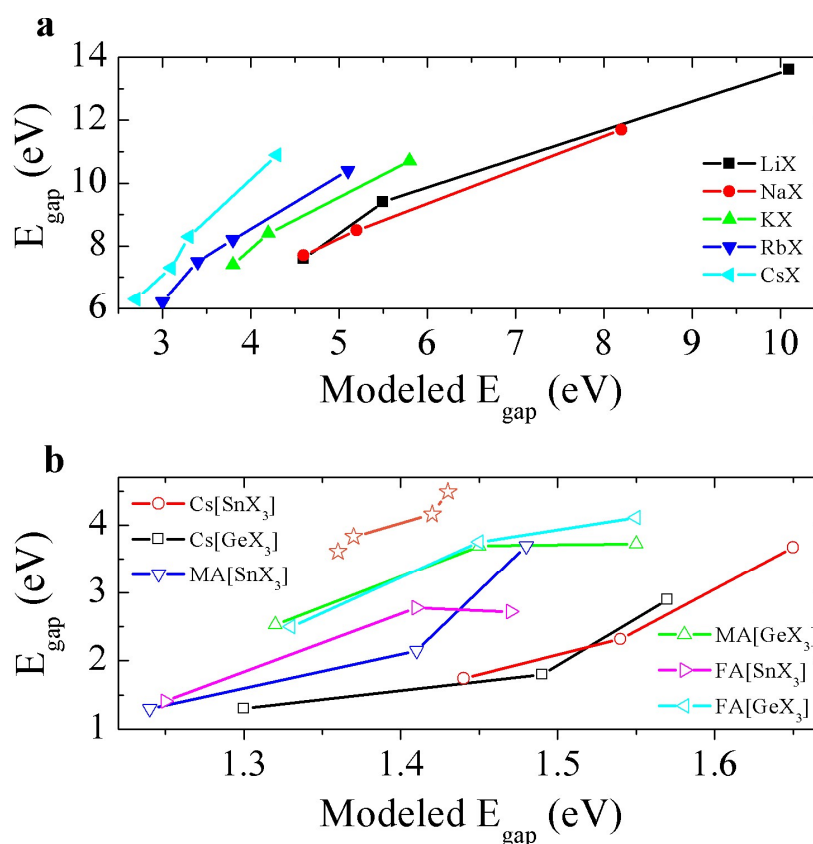


Figure 3. Available experimental or HSE calculated band gaps (y-axis) of (a) alkali halide crystals and (b) super alkali halide crystals against the band gaps computed in our model (x-axis) using the Pauling-type ionic radii. Similar behavior is observed when using the Shannon-type ionic radii. MA and FA stand for CH_3NH_3 and $\text{HC}(\text{NH}_2)_2$, respectively. In each curve, X = Cl, Br, I correspond to the data points from right to left. The band gap decreases in the order of X = Cl, Br, I, except for FASnCl_3 and FASnBr_3 , where our PBE and HSE calculations find that the band gap of the former is slightly smaller than that of the latter (Supporting Table S13). We reckon this may be due to the approximation of the crystal lattice obtained from the molecular dynamics of FASnBr_3 as tetragonal (see the Supporting Figure S5 and S6^[28]). The band gaps of $\text{A}[\text{M}(\text{BH}_4)_3]$ (open stars) decrease in the order of $\text{FA}[\text{Ge}(\text{BH}_4)_3]$, $\text{MA}[\text{Ge}(\text{BH}_4)_3]$, $\text{FA}[\text{Sn}(\text{BH}_4)_3]$ and $\text{MA}[\text{Sn}(\text{BH}_4)_3]$. All these band gap values are given in the Supporting Table S13^[28].

As shown in Supporting Table S13, the ionic radii of (super/hyper) halogens in their pyramidal forms are significantly smaller than their radii in the symmetric form. By assuming that the cation radii change little, this leads to larger radius ratio in the low-symmetry phase of the material. According to our model, this corresponds to larger band gaps compared to the high-symmetry phase. Different hybrid perovskites may show different phases under the same ambient conditions. For example, both $\text{CH}_3\text{NH}_3\text{SnBr}_3$ and $\text{CH}_3\text{NH}_3\text{SnI}_3$ show the high-symmetry tetragonal and cubic phases at room temperature, while $\text{CH}_3\text{NH}_3\text{SnCl}_3$ shows the low-symmetry triclinic or monoclinic phase. Therefore, it is fitting to represent the band gap of a material within a range with the value of the cubic phase as the lower bound and the value of the low-symmetry phase as the upper bound. Indeed, as observed in the available experiments and calculations, the cubic phase of a hybrid perovskite shows a smaller band gap compared to its low-symmetry phases.

Our simple ionic model has some apparent limitations in describing the real crystals. For example, in the three dimensions, the shape of the potential is not a simple square well and the lattice parameter is not simply the addition of the two ionic radii. However, such deficiency is partially compensated by the use of hybrid-DFT computed ionicity and the defined ionic radii based on the crystalline data. Besides indicating the difference between high-symmetry and low-symmetry crystal phases with regular octahedral and pyramidal forms, respectively (as discussed above), the ionic radii contain another important piece of information of the crystalline structure, i.e. the coordination number of ions inside the crystal. In the definition of Shannon-like ionic radii, the defined ionic radii for the cations are larger in the case of 8-fold coordination than those in the case of 6-fold coordination, while the ionic radii of the anions in the former case are smaller than the ones in the latter, as shown in Supporting Table S5^[28]. Such trend is due to the fact that, in a hard-sphere model, a large cation is able to attract more small anions to lower the energy with less repulsion between the neighboring anions. Although such trend does not apply for the Pauling's model in Eq. (S58)-(S62) in Supporting

Information ^[28], where ions are not touching each other, different coordination numbers do result in different sets of ionic radii as shown in the Supporting Table S8 and S9.

Also, the model does not include the relativistic effects such as spin-orbit coupling which has been found to be present in real materials ^[33, 44-46]. Our DFT studies which agree with previous calculations ^[33, 44-45] show that the effect of the spin-orbit coupling on the band-gap values for the lead-free hybrid perovskites is not large. For materials involving Sn, the typical change is of the order of 0.3 eV while that with Ge it is of the order of 0.06 eV. Considering these factors, the agreement between the band gaps in our model and the experimental (or hybrid-DFT calculated) values is indeed remarkable, underscoring the ionic character of the studied materials. The relativistic effects will become important to determine the band gaps of hybrid perovskites with lead (Pb), which results in a relatively large downshift of the valence band and increases the band gap of MAPbI₃ compared to that of MASnI₃ ^[44]. Indeed, if only the ionic radii (Pauling type = 2.75 Å for [PbI₃]⁻) and the bonding ionicity (in Supporting Table S2 ^[28] for MAPbI₃) are considered as in our model, the calculated band gap of MAPbI₃ is 1.25 eV -- slightly smaller than 1.26 eV of MASnI₃.

2.4. Stability of Hybrid Perovskites Exposed to Moisture

It is well known that all the alkali halides are hygroscopic. Therefore, it is natural that hybrid perovskites viewed as “super” alkali halide crystals are also found to be hygroscopic ^[6, 11, 32, 47-49]. The most widely studied hybrid-perovskite solar cell so far, CH₃NH₃PbI₃ ^[6, 32], is unstable when exposed to moisture and concentrated sunlight and readily degrades to PbI₂ and loses its photovoltaic function ^[47-49]. Grotthuss mechanism ^[50] has been proposed to be responsible for this degradation ^[48-49]. According to this mechanism one of the protons H⁺ of the organic cation [CH₃NH₃]⁺ hops on to the water molecule causing the proton of the water molecule on the other side to transfer to iodine. Consequently a strong acid HI is formed

leaving a yellow powder of PbI_2 . Effort has been made to improve the durability of the material by partially replacing iodine with bromine ^[6, 47]. Although such replacement slightly increases the band gap, it is shown to result in much better stability of the solar cell ^[6, 47].

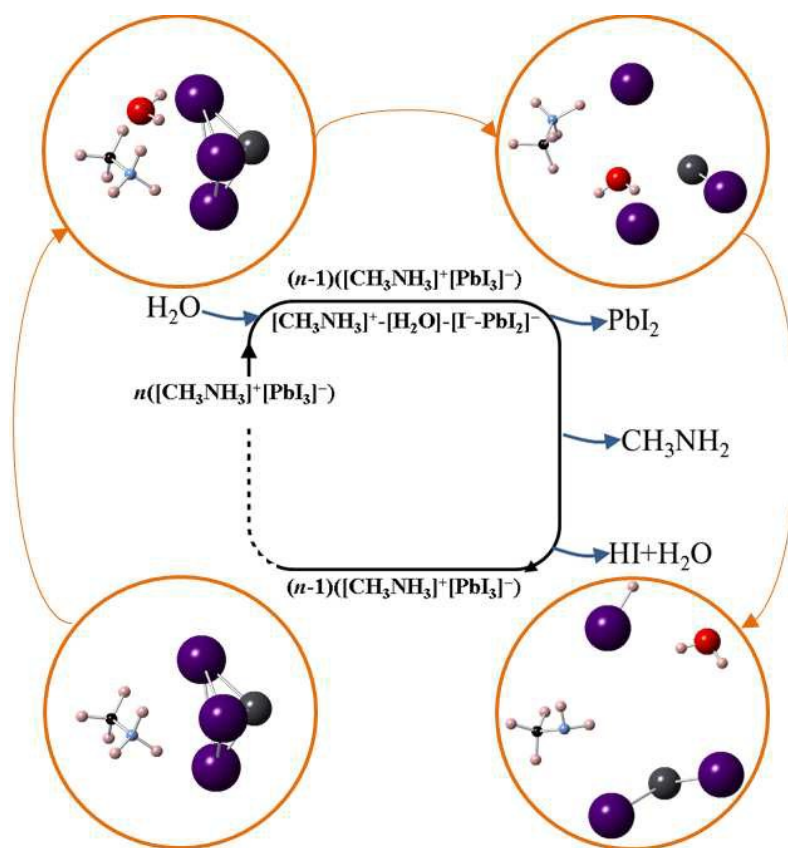


Figure 4. Degradation mechanism of $\text{CH}_3\text{NH}_3\text{PbI}_3$ exposed to moisture. The ball-and-stick plots (Pb: lead black; I: purple; N: cyan; C: black; O: red; H: pink) in the circles demonstrate the process in sequence as indicated by the arrows. It starts with the reactant as one water molecule is trapped between the super alkali $[\text{CH}_3\text{NH}_3]^+$ and super halogen $[\text{PbI}_3]^-$ and ends up with products of PbI_2 , CH_3NH_2 , HI and H_2O .

To explore the degradation process, we have carried out *ab initio* molecular dynamics simulations (see Method) for a cluster model of $\text{CH}_3\text{NH}_3\text{PbI}_3 \cdot \text{H}_2\text{O}$. Armed with its small size and polarized configuration, a water molecule is found to be easily trapped between A^+ and $[\text{MX}_3]^-$ ions with the negative oxygen attracted to the positive super-alkali and the positive

hydrogen attracted to the negative super-halogen. This weakens the ionic bonding between the two super-ions (see Figure 4 and Supporting Figure S13 ^[28]). However, in our calculations, we did not find a transition state associated with the Grotthuss mechanism. The molecular dynamics simulations (see the animation in Supporting Information ^[28]) show that at high temperature the water molecule enters between two iodine atoms of the $[\text{PbI}_3]^-$ anion, turning its oxygen towards one of the them. Given the large negative charge on both the oxygen and the iodine atom, the water molecule pushes the iodine away. The isolated and highly negative iodine then seizes a proton from the NH_3 group in the organic cation to form HI which then starts to adhere to the water molecule. The leftovers are PbI_2 and CH_3NH_2 . This is demonstrated schematically in Figure 4. Such mechanism is consistent with the findings from molecular dynamics simulations on a crystalline system of $\text{CH}_3\text{NH}_3\text{PbI}_3$ ^[51], suggesting that the hygroscopicity of the hybrid perovskite is indeed largely determined by the properties of the super-ions and their bonding.

Based on these findings, several strategies are formed to counter the degradation. The first one is to lower the binding energy between the water molecule and the super-alkali halide, so that the water molecule does not get trapped between the ions easily. For the elementary halogen X in $[\text{MX}_3]^-$, we can do little to change the amount of charge on X to further reduce its Coulombic attraction to the water molecule. However, with X replaced by super-halogens such as BH_4 , the negative charge is now shared by many H atoms ^[52]. This in turn significantly reduces the charge on each atom, hence reducing its attraction to the water molecule. This can also reduce the force exerted by oxygen in the water molecule on these ions upon thermal excitations. Indeed, the hybrid perovskites consisting of hyper-halogens $[\text{Ge}/\text{Sn}(\text{BH}_4)_3]^-$ proposed in the paper show significantly reduced (about 20 % off) binding energy with the water molecule compared to the materials with super halogens $[\text{Ge}/\text{SnX}_3]^-$, as shown in Supporting Table S14. The NBO analysis in Supporting Sec. XI confirms that

the -1 charge in $[\text{Ge/Sn}(\text{BH}_4)_3]^-$ is shared by 12 hydrogen atoms, which makes each hydrogen only show a fraction of charge, while the negative boron ions are shielded by the surrounding hydrogens atoms.

The second strategy is to enhance the bonding between M and X within the $[\text{MX}_3]^-$ super-halogen so that the water molecule cannot easily remove one of the X atoms from the group. We find that replacing iodine with bromine in $\text{CH}_3\text{NH}_3\text{PbI}_3$ as was done in the experiments^[6, 47] does exactly that. Although such replacement will increase the binding energy of the water molecule to the super-alkali halide (see Supporting Table S14^[28]), the bonding between Pb and Br would be significantly stronger than that between Pb and I, given the large charge states of Pb and Br and the shorter bond lengths between them (Supporting Table S14^[28]). The stronger bond strength of Pb-Br than Pb-I is also confirmed by the significantly higher frequencies of the vibrational modes that involve the bond stretching motion, as shown by the infrared spectra in Supporting Sec. XII. The hyper-halogen $[\text{M}(\text{BH}_4)_3]^-$ also shows good sign in this regard, having the averaged bond length of M-B even smaller than that of M-Br, as shown in Supporting Table S14^[28].

The third strategy is to replace the organic cation of the hybrid perovskites with inorganic cation so as to avoid the NH_3 group entirely. An ideal candidate should have comparably large size and proper electronegativity in order to yield small band gaps, as indicated in this study. In addition, the candidate should possess intrinsic dipole moment which is considered to be vital for the exceptionally long diffusion distance (up to order of a micrometer) of the photo-excited carriers in the materials^[13]. We examined one possible candidate of an inorganic super alkali $[\text{Li}_3\text{O}]^+$ ^[24] that has a planar configuration as shown in Supporting Sec. XIII. However, our molecular dynamics simulation shows that $\text{Li}_3\text{O}[\text{Ge/SnI}_3]$ and their hyper-halogen analogues $\text{Li}_3\text{O}[\text{Ge/Sn}(\text{BH}_4)_3]$ quickly undergo phase transition to some non-perovskite phase after reaching the initial equilibrium as shown in Supporting Sec. IV. It will

be useful to explore if other inorganic super-alkalis may produce a more desirable result. We will continue to investigate this possibility.

2.5. Colorful Hybrid Perovskites

According to Figure 2a, the hyper-halogens $[\text{Ge}(\text{BH}_4)_3]^-$ and $[\text{Sn}(\text{BH}_4)_3]^-$ have very similar ionic radii as those of $[\text{GeBr}_3]^-$ and $[\text{SnBr}_3]^-$, respectively. Experimentally, $[\text{MBr}_3]^-$ has been used to replace $[\text{MI}_3]^-$ in hybrid perovskites and shows great miscibility^[6, 11]. Therefore, the crystal lattice should also be able to accommodate the size of the hyper-halogens $[\text{M}(\text{BH}_4)_3]^-$ when $[\text{MI}_3]^-$ is partially replaced. Moreover, as indicated by the dotted lines in Figure 2a, the hyper-halogens show almost identical ionicity with the $[\text{MI}_3]^-$ ion. Such property can reassure chemical stability and will not change the band gap position too much upon the partial replacement (as discussed in Sec. 2.1).

$[\text{CH}_3\text{NH}_3/\text{HC}(\text{NH}_2)_2][\text{M}(\text{BH}_4)_3]$ have band gaps in the range of 3.0-4.5 eV, as shown in Figure 3. The relatively large band gaps of $[\text{CH}_3\text{NH}_3/\text{HC}(\text{NH}_2)_2][\text{M}(\text{BH}_4)_3]$ compared to those of $[\text{CH}_3\text{NH}_3/\text{HC}(\text{NH}_2)_2][\text{MX}_3]$ are due to the different electron states of the top (bottom) valence (conduction) band. For the latter materials, the major contributions come from the 4*p* electrons of the halogen X atom and the 4*s*/4*p* or 5*s*/5*p* electrons of the metal atom. For the former materials, however, the contributions are from the less-energetic and less-diffusive *sp* electrons of hydrogen and boron. These are shown in the partial densities of states in Supporting Sec. IX^[28]. Such effects are excluded from our simple model which only considers the ionicity and the ionic radii. Indeed, as shown in Figure 3, the absolute values of the band gaps of $[\text{CH}_3\text{NH}_3/\text{HC}(\text{NH}_2)_2][\text{M}(\text{BH}_4)_3]$ computed from our model are similar to those of $[\text{CH}_3\text{NH}_3/\text{HC}(\text{NH}_2)_2][\text{MI}_3]$ and $[\text{CH}_3\text{NH}_3/\text{HC}(\text{NH}_2)_2][\text{MBr}_3]$.

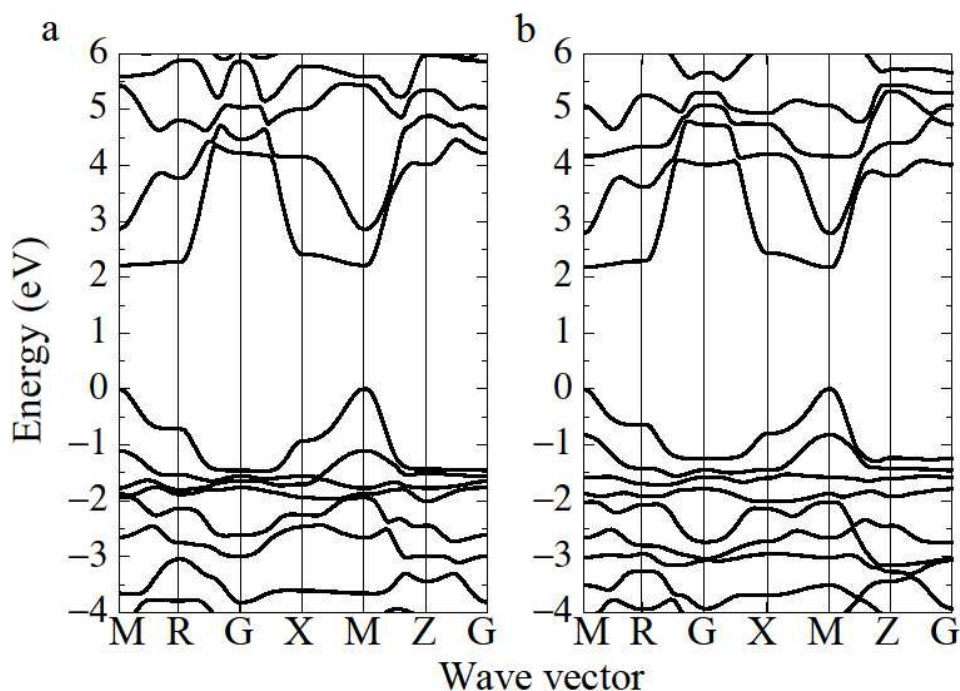


Figure 5. HSE calculated electronic band structures of (a) $\text{HC}(\text{NH}_2)_2[\text{GeI}_2(\text{BH}_4)]$ and (b) $\text{CH}_3\text{NH}_3[\text{GeI}_2(\text{BH}_4)]$ using the lattice parameters of $\text{HC}(\text{NH}_2)_2[\text{GeI}_3]$ and $\text{CH}_3\text{NH}_3[\text{GeI}_3]$, respectively, but with relaxed ionic positions. The direct band gaps are present at the M point. The "G" point denotes the Γ point.

Based on the above discussions, sequential replacement of I in $[\text{MI}_3]^-$ or Br in $[\text{MBr}_3]^-$ by the super-halogen, BH_4 , can lead to colorful hybrid perovskites, even extending absorption into the ultra violet region. The band gap of 1.3 and 1.41 eV of $\text{CH}_3\text{NH}_3\text{SnI}_3$ and $\text{HC}(\text{NH}_2)_2\text{SnI}_3$, respectively, can reach 4.16 eV in $\text{CH}_3\text{NH}_3\text{Ge}(\text{BH}_4)_3$ and 4.49 eV in $\text{HC}(\text{NH}_2)_2\text{Ge}(\text{BH}_4)_3$. Since the DFT (both PBE and HSE) as well as our model calculated band gaps of $\text{HC}(\text{NH}_2)_2[\text{Ge}(\text{BH}_4)_3]$ and $\text{CH}_3\text{NH}_3[\text{Ge}(\text{BH}_4)_3]$ are larger than those of $\text{HC}(\text{NH}_2)_2[\text{Sn}(\text{BH}_4)_3]$ and $\text{CH}_3\text{NH}_3[\text{Sn}(\text{BH}_4)_3]$ (Supporting Table S13^[28]), we expect that the alloys, $\text{HC}(\text{NH}_2)_2[\text{GeI}_2(\text{BH}_4)]$ and $\text{CH}_3\text{NH}_3[\text{GeI}_2(\text{BH}_4)]$, should have larger band gaps than their Sn counterparts, as shown by the PBE results in Supporting Sec. XIV. Figure 5 shows that the HSE calculated direct band gaps of $\text{HC}(\text{NH}_2)_2[\text{GeI}_2(\text{BH}_4)]$ and $\text{CH}_3\text{NH}_3[\text{GeI}_2(\text{BH}_4)]$ are 2.17 and 2.22 eV, respectively, which are slightly smaller than those of $\text{HC}(\text{NH}_2)_2\text{GeI}_3$ and $\text{CH}_3\text{NH}_3\text{GeI}_3$ (see Supporting Table S13). Note that we used the lattice parameters of

$\text{HC}(\text{NH}_2)_2[\text{GeI}_3]$ and $\text{CH}_3\text{NH}_3[\text{GeI}_3]$ for the corresponding admixtures whose lattices are expected to be smaller given the smaller ionic radius of $[\text{Ge}(\text{BH}_4)_3]^-$ compared to $[\text{GeI}_3]^-$. Since the hybrid perovskites are supposed to have positive band-gap deformation potentials (i.e. the band gap will increase with expanded lattice) ^[49], our calculated band gaps of the admixtures are expected to be larger than the real values. These results suggest that alloys $\text{HC}(\text{NH}_2)_2[\text{SnI}_2(\text{BH}_4)]$ and $\text{CH}_3\text{NH}_3[\text{SnI}_2(\text{BH}_4)]$ having band gaps lower than 2 eV is highly possible.

To further see the miscibility of the alloy from the band gap, we extract the bowing factor ^[6, 53] from the DFT calculated band gaps of $\text{AM}[\text{I}_{1-x}(\text{BH}_4)_x]_3$ ($\text{A} = \text{MA}$ and FA ; $\text{M} = \text{Ge}$ and Sn) with $x = 0, 1/3, 2/3, 1$, as shown in the Supporting Sec. XV ^[28]. The bowing factors from DFT-PBE calculated band gaps are 2.45 eV and 2.97 eV for $\text{MAGe}[\text{I}_{1-x}(\text{BH}_4)_x]_3$ and $\text{FAGe}[\text{I}_{1-x}(\text{BH}_4)_x]_3$, respectively. The corresponding bowing factors from HSE calculated band gaps are slightly larger -- 2.88 eV and 3.39 eV. For $\text{MASn}[\text{I}_{1-x}(\text{BH}_4)_x]_3$ and $\text{FASn}[\text{I}_{1-x}(\text{BH}_4)_x]_3$, the bowing factors from DFT-PBE calculated band gaps are 1.44 eV and 2.27, respectively. Although these values are larger than the tiny bowing factor (0.33 eV) of $\text{MAPb}[\text{I}_{1-x}\text{Br}_x]_3$ [6], they are comparable to the bowing factors of the well-known ternary semiconductors $\text{Al}(\text{P},\text{Sb})$ (2.7~3.6 eV), $\text{Ga}(\text{P},\text{Sb})$ (2.6~2.7 eV), $\text{In}(\text{P},\text{Sb})$ (1.9 eV) and $\text{Ga}(\text{As},\text{Sb})$ (1.2~1.4 eV) ^[53]. Thus, these studied alloys with iodine and BH_4 should have good miscibility.

3. Conclusion

In this study, we introduce a new vision of hybrid perovskites as super crystals mimicking the alkali halides where the alkali and halogen atoms are replaced by super-alkalis and super-halogens, respectively. Based on this, we show that changing the building blocks

from atomic ions to super-ions empower hybrid perovskites with unusual properties. We find that the basic properties of the materials are decided by the defined ionic radii and the bonding ionicity of the super-ions. The degradation mechanism of the materials when exposed to moisture has been identified and counter strategies are given. These new findings open the door to design new colorful lead-free hybrid perovskites that are both stable and versatile. Moreover, we expect the current study to trigger recognition of complex materials as super crystals where super-ions form the building blocks. The recently synthesized superionic conductivity materials $[\text{Li}_3\text{O}]\text{X}$ ($\text{X} = \text{halogen}$)^[54] and $\text{M}[\text{B}_{12}\text{H}_{12}]$ ($\text{M} = \text{alkali}$)^[55] are some examples of such, where $[\text{Li}_3\text{O}]^+$ and $[\text{B}_{12}\text{H}_{12}]^{2-}$ are all super-ions. Based on such recognition, general rules to understand and modify the functionality of complex materials can be generated by drawing analogy with their simpler cousins built from elementary ions, as demonstrated in this paper.

4. Computational Methods

Density Functional Theory (DFT) Calculations of Clusters. Equilibrium structures, total energies, and electronic properties of the cations and anions forming hybrid perovskites are computed using density functional theory and hybrid exchange-correlation functional based on the Becke three parameter Lee-Yang-Parr (B3LYP) method. All cluster calculations are carried out using the Gaussian 03 package^[56]. The electron affinity and ionization energies of the super-alkali and super-halogen ions are calculated using their optimized geometry in corresponding charge states. The ionicities of various molecular building blocks are determined from Equation (S1)-(S3) (Supplementary Information^[28]) using vertical ionization energy and vertical electron affinity associated with the optimized geometry of the neutral states^[57]. The basis set used for halogen ions as well as H and B is 6-311+G*. For Ge, Sn and Pb, aug-cc-pVDZ basis sets are used. Frequency calculations are conducted for all

clusters to ensure that there are no imaginary frequencies and that the structures belong to minima in the potential energy landscape. The natural bond orbital (NBO) analysis is carried out for the fully optimized structures. The binding energies between the water molecule and the super-alkali halide molecules are calculated using the counterpoise correction to the basis set superposition error (BSSE).

Ab initio Molecular Dynamics Simulations. Molecular dynamics (MD) simulations of hybrid perovskite crystals are performed using the projector augmented wave (PAW) method^[58] and the Perdew-Burke-Ernzerhof generalized gradient approximation (PBE-GGA)^[59] for exchange-correlation functional embedded in the VASP package^[60-61]. The Parrinello-Rahman dynamics of constant pressure and constant temperature (NpT) with Langevin thermostat^[62] is used, allowing both the size and the shape of the cells to change during simulation. External pressure and temperature are set to the ambient condition (0.001 GPa and 300 K). A $3\times 3\times 3$ super cell with a pseudo-cubic unit containing one AMX_3 molecule is used in each simulation. The simulations are conducted with normal precision (in VASP) and a tolerance of 1×10^{-5} eV for the SCF cycle without any symmetry constraints. A time step of 0.001 ps is chosen. The atomic trajectory data are collected every 10 steps for 4 ps after the free energy and temperature reach equilibrium. An averaged configuration of each material is then computed using these data, subject to X-ray diffraction pattern analysis. To simulate the interaction between the water molecule and a super alkali halide molecule, long-distance van der Waals interactions are included by using Grimme's DFT+D2 scheme^[63]. The simulations are conducted using NVT ensemble with Nose-Hoover thermostat. A large $30\times 30\times 30$ Å cell is used to contain the energy-relaxed cluster with one water molecule binding to an AMX_3 molecule. The simulations are conducted with 'normal' precision (in VASP) and a tolerance of 1×10^{-5} eV for the SCF cycle without any symmetry constraints. The time step is set to 0.001 ps and atomic trajectories are collected every 20 steps. Simulations at both low

temperature (300 K) and high temperature (1000 K) phase are carried out and are then put into animation.

DFT-Based Electronic and Dynamic Lattice Calculations on Crystals. *Ab initio* calculations for the crystalline phase are performed with the projector augmented wave (PAW)^[58] and the Perdew-Burke-Ernzerhof generalized gradient approximation (PBE-GGA)^[59] using the VASP package^[60-61]. The electronic structure calculations are performed with and without the spin-orbit coupling (SOC). Range-separated hybrid functional, HSE06^[64], is also used in the calculations to generate reliable band gaps^[65]. The plane-wave cutoff energy is set to 600 eV. Monkhorst-Pack 6×6×6 k-meshes^[66] are adopted. For each material, a pseudo-cubic unit cell is used with the crystal structures and lattice parameters obtained from the averaged configuration obtained from the MD simulation under ambient conditions. The atomic positions are relaxed until the residual force on each atom is less than 0.005 eV/Å and the total energy change is less than 1×10^{-5} eV. For the lattice dynamics calculations, these tolerances change to 0.0001 eV/Å and 1×10^{-8} eV, respectively. Phonons are computed on a 6×6×6 grid and then interpolated for arbitrary q point in the Brillouin zone.

ToC: Hybrid perovskites viewed as super alkali halides with alkali and halogen ions replaced by super alkalis and super halogens, respectively. The basic properties of these materials are determined by the bonding ionicity and effective ionic radii of the super-ions. New colorful hybrid perovskites can be invented with super-ions as the building block.



Acknowledgements

This work is supported in part by the U. S. Department of Energy, Office of Basic Energy Sciences, Division of Materials Sciences and Engineering under Award # DE-FG02-96ER45579. Resources of the National Energy Research Scientific Computing Center supported by the Office of Science of the U.S. Department of Energy under Contract No. DE-AC02-05CH11231 is also acknowledged.

Reference

- [1] Mitzi, D. B., Field, C. A., Harrison, W. T. A. and Guloy, A. M. Conducting tin halides with a layered organic-based perovskite structure. *Nature* 369, 467 (1994).
- [2] Lee, M. M., Teuscher, J., Miyasaka, T., Murakami, T. N. and Snaith, H. J. Efficient hybrid solar cells based on meso-superstructured organometal halide perovskites. *Science* 338, 643 (2012).
- [3] Etgar, L., Gao, P., Xue, Z., Peng, Q., Chandiran, A. K., Liu, B., Nazeeruddin, M. K. and Graetzel, M. Mesoscopic $\text{CH}_3\text{NH}_3\text{PbI}_3/\text{TiO}_2$ heterojunction solar cells. *J. Am. Chem. Soc.* 134, 17396 (2012).

- [4] Hodes, G. Perovskite-based solar cells. *Science* 342, 317 (2013).
- [5] Loi, M. A. and Hummelen, J. C. Hybrid solar cells: perovskites under the sun. *Nature Materials* 12, 1087 (2013).
- [6] Noh, J. H., Im, S. H., Heo, J. H., Mandal, T. N. and Seok, S. I. Chemical management for colourful, efficient, and stable inorganic-organic hybrid nanostructured solar cells. *Nano Letters* 13, 1764 (2013).
- [7] Snaith, J. H. Perovskites: the emergence of a new era for low-cost, high-efficiency solar cells. *J. Phys. Chem. Lett.* 4, 3623 (2013).
- [8] Park, N. G. Organometal perovskite light absorbers toward a 20% efficiency low-cost solid-state mesoscopic solar cell. *J. Phys. Chem. Lett.* 4, 2423 (2013).
- [9] Bisquert, J. The swift surge of perovskite photovoltaics. *J. Phys. Chem. Lett.* 4, 2597 (2013).
- [10] Lotsch, B. V. New light on an old story: perovskites go solar. *Angewandte Chemie International Edition* 53, 635 (2014).
- [11] Hao, F., Stoumpos, C. C., Cao, D. H., Chang, R. P. H. and Kanatzidis, M. G. Lead-free solid-state organic-inorganic halide perovskite solar cells. *Nature Photonics* 8, 489 (2014).
- [12] Tan, Z., Moghaddam, R. S., Lai, M. L., Docampo, P., Higler, R., Deschler, F., Price, M., Sadhanala, A., Pazos, L. M., Credgington, D., Hanusch, F., Bein, T., Snaith, H. J. and Friend, R. H. Bright light-emitting diodes based on organometal halide perovskite. *Nature Nanotechnology* 9, 687 (2014).
- [13] Xing, G., Mathews, N., Lim, S. S., Yantara, N., Liu, X., Sabba, D., Graetzel, M., Mhaisalkar, S. and Sum, T. C. Low-temperature solution-processed wavelength-tunable perovskites for lasing. *Nature Materials* 13, 476 (2014).
- [14] Deschler, F., Price, M., Pathak, S., Klintberg, L. E., Jarausch, D., Higler, R., Huettner, S., Leijtens, T., Stranks, S. D., Snaith, H. J., Atatuere, M., Phillips, R. T. and Friend, R. H.

- High photoluminescence efficiency and optically pumped lasing in solution-processed mixed halide perovskite semiconductors. *J. Phys. Chem. Lett.* 5, 1421 (2014).
- [15] Yamada, K., Mikawa, K., Okuda, T. and Knight, K. S. Static and dynamic structures of $\text{CD}_3\text{ND}_3\text{GeCl}_3$ studied by TOF high resolution neutron powder diffraction and solid state NMR. *J. Chem. Soc., Dalton Trans.*, 2112 (2002).
- [16] Thiele, G., Rotter, H. W. and Schmidt, K. D. Die kristallstrukturen und phasentransformationen von RbGeBr_3 . *Z. Anorg. Allg. Chem.* 559, 7 (1988).
- [17] Depmeier, W. and Moeller, A. The structure of antiferroelectric tetramethylammonium trichlorogermanate(II) at room temperature. *Acta Crystallogr. Sect. B* 36, 803 (1980).
- [18] Yamada, K., Nose, S., Umehara, T., Okuda, T. and Ichiba, S. ^{81}Br NQR and ^{119}Sn Mössbauer study for MSnBr_3 ($\text{M} = \text{Cs}$ and CH_3NH_3). *Bull. Chem. Soc. Jpn.* 61, 4265 (1988).
- [19] Yamada, K., Funabiki, S., Horimoto, H., Matsui, T., Okuda, T. and Ichiba, S., Structural phase transitions of the polymorphs of CsSnI_3 by means of Rietveld analysis of the X-ray diffractions. *Chem. Lett.*, 801 (1991).
- [20] Feng, J. and Xiao, B. Crystal structures, optical properties, and effective mass tensors of $\text{CH}_3\text{NH}_3\text{PbX}_3$ ($\text{X} = \text{I}$ and Br) phases predicted from HSE06. *J. Phys. Chem. Lett.* 5, 1278 (2014).
- [21] Lin, Q., Armin, A., Nagiri, R. C. R., Burn, P. L. and Meredith, P. Electro-optics of perovskite solar cells. *Nature Photonics* 9, 106 (2015).
- [22] Gutsev, G. L. and Boldyrev, A. I. DVM $X\alpha$ calculations on the electronic structure of “superalkali” cations. *Chem. Phys. Lett.* 92, 262 (1982).
- [23] Gutsev, G. L. and Boldyrev, A. I. DVM $X\alpha$ calculations on the ionization potentials of $\text{MX}^-_{(k+1)}$ complex anions and the electron-affinities of MK_{k+1} superhalogens. *Chem. Phys. Lett.* 56, 277 (1981).

- [24] Giri, S., Behera, S. and Jena, P. Superalkalis and superhalogens as building blocks of supersalts. *J. Phys. Chem. A* 118, 638 (2014).
- [25] Willis, M., Goetz, M., Kandalam, A. K., Gantefoer, G. F. and Jena, P. Hyperhalogens: Discovery of a new class of highly electronegative species. *Angew. Chem. Int. Ed.* 49, 8966 (2010).
- [26] Knight, D. A. et al. Synthesis, characterization, and atomistic modeling of stabilized highly pyrophoric $\text{Al}(\text{BH}_4)_3$ via the formation of the hypersalt $\text{K}[\text{Al}(\text{BH}_4)_4]$. *J. Phys. Chem. C* 117, 19905 (2013).
- [27] Paduani, C., Wu, M. M., Willis, M. and Jena, P. Theoretical study of the stability and electronic structures of $\text{Al}(\text{BH}_4)_{n=1-4}$ and $\text{Al}(\text{BF}_4)_{n=1-4}$ and their hyperhalogen behavior. *Phys. Chem. A* 115, 10237 (2011).
- [28] Supporting Information.
- [29] Phillips, J. C. Ionicity of the chemical bond in crystals. *Rev. Mod. Phys.* 42, 317 (1970).
- [30] Poole, R. T., Jenkin, J. G., Leckey, R. C. G. and Liesegang, J. Ionicity and photoelectron emission: The alkali halides. *Chem. Phys. Lett.* 26, 514 (1974).
- [31] Fajans, K. Struktur und deformation der elektronenhüllen in ihrer bedeutung für die chemischen und optischen eigenschaften anorganischer verbindungen. *Naturwiss* 11, 165 (1923).
- [32] Ogomi, Y., Morita, A., Tsukamoto, S., Saitho, T., Fujikawa, N., Shen, Q., Toyoda, T., Yoshino, K., Pandey, S. S., Ma, T. and Hayase, S. $\text{CH}_3\text{NH}_3\text{Sn}_x\text{Pb}_{(1-x)}\text{I}_3$ perovskite solar cells covering up to 1060 nm. *J. Phys. Chem. Lett.* 5, 1004 (2014).
- [33] Even, J., Pedesseau, L., Jancu, J. and Katan, C. Importance of spin-orbit coupling in hybrid organic/inorganic perovskites for photovoltaic applications. *J. Phys. Chem. Lett.* 4, 2999 (2013).

- [34] Pauling, L. The influence of relative ionic sizes on the properties of ionic compounds. *J. Am. Chem. Soc.* 50, 1036 (1928); Atomic radii and interatomic distances in metals. *J. Am. Chem. Soc.* 69, 542 (1947).
- [35] Yamada, K., Kuranaga, Y., Ueda, K., Goto, S., Okuda, T. and Furukawa, Y. Phase transition and electric conductivity of ASnCl_3 (A = Cs and CH_3NH_3). *Bull. Chem. Soc. Jpn.* 71, 127 (1998).
- [36] Yamada, K., Isobe, K., Tsuyama, E., Okuda, T., Furukawa, Y. Chloride ion conductor $\text{CH}_3\text{NH}_3\text{GeCl}_3$ studied by Rietveld analysis of X-ray diffraction and ^{35}Cl NMR. *Solid State Ionics* 79, 152 (1995).
- [37] Stoumpos, C. C., Malliakas, C. D. and Kanatzidis, M. G. Semiconducting tin and lead iodide perovskites with organic cations: Phase transitions, high mobilities, and near-infrared photoluminescent properties. *Inorg. Chem.* 52, 9019 (2013).
- [38] Schouwink, P., Ley, M. B., Tissot, A., Hagemann, H., Jensen, T. R., Smrčok, L. and Černý, R. Structure and properties of complex hydride perovskite materials. *Nature Communication* 5, 5706 (2014).
- [39] Shannon, R. D. Revised effective ionic radii and systematic studies of interatomic distances in halides and chalcogenides. *Acta. Cryst. A* 32, 751 (1976).
- [40] Pauling, L. The influence of relative ionic sizes on the properties of ionic compounds. *J. Am. Chem. Soc.* 50, 1036 (1928).
- [41] Andreev, S. V., Letokhov, V. S., Mishin, V. I. Laser resonance photoionization spectroscopy of Rydberg levels in Fr. *Phys. Rev. Lett.* 59, 1274 (1987).
- [42] Willis, M., Goetz, M., Kandalam, A. K., Gantefoer, G. F. and Jena, P. Hyperhalogens: Discovery of a new class of highly electronegative species. *Angew. Chem. Int. Ed.* 49, 8966 (2010).
- [43] Lyddane, R. H., Sachs, R. G. and Teller, E. On the polar vibrations of alkali halides. *Phys. Rev.* 59, 673 (1941).

- [44] Umari, P., Mosconi, E. and De Angelis, F. Relativistic GW calculations on $\text{CH}_3\text{NH}_3\text{PbI}_3$ and $\text{CH}_3\text{NH}_3\text{SnI}_3$ perovskites for solar cell applications. *Sci. Rep.* 4, 4467 (2014).
- [45] Katan, C., Pedesseau, L., Kepenekian, M., Rolland, A. and Even, J. Interplay of spin-orbit coupling and lattice distortion in metal substituted 3D tri-chloride hybrid perovskites. *J. Mater.Chem.A* 3, 9232 (2015).
- [46] Amat, A., Mosconi, E, Ronca, E., Quarti, C., Umari, P., Nazeeruddin, Md K., Graetzel, M. and De Angelis, F. Cation-induced band-gap tuning in organohalide perovskites: Interplay of spin-orbit coupling and octahedral tilting. *Nano Lett.* 14, 3608 (2014).
- [47] Misra, R. K., Aharon, S., Li, B., Mogilyansky, D., Visoly-Fisher, I., Etgar, L. and Katz, E. A. Temperature- and component-dependent degradation of perovskite photovoltaic materials under concentrated sunlight. *J. Phys. Chem. Lett.* 6, 326 (2015).
- [48] Deretzis, I., Alberti, A., Pellegrino, G., Smecca, E., Giannazzo, F., Sakai, N., Miyasaka, T. and La Magna, A. Atomistic origins of $\text{CH}_3\text{NH}_3\text{PbI}_3$ degradation to PbI_2 in vacuum. *Appl. Phys. Lett.* 106, 131904 (2015).
- [49] Frost, J. M., Butler, K. T., Brivio, F., Hendon, C. H., van Schilfgaarde, M. and Walsh, A. Atomistic origins of high-performance in hybrid halide perovskite solar cells. *Nano Lett.* 14, 2584 (2014).
- [50] Agmon, N. The Grotthuss mechanism. *Chem. Phys. Lett.* 244, 456 (1995).
- [51] Mosconi, E., Azpiroz, J. M. and Angelis, F. D. Ab initio molecular dynamics simulations of methylammonium lead iodide perovskite degradation by water. *Chem. Mater.* 27, 4885 (2015).
- [52] Jena, P. Beyond the periodic table of elements: The role of superatoms. *J. Phys. Chem. Lett.* 4, 1432 (2013).
- [53] J. Piprek, *Semiconductor Optoelectronic Devices Introduction to Physics and Simulation*, Academic Press (2002).

- [54] Zhao, Y. and Daemen, L. L. Superionic conductivity in lithium-rich anti-perovskites. *J. Am. Chem. Soc.* 134, 15042 (2012).
- [55] He, L., Li, H., Nakajima, H., Tumanov, N., Filinchuk, Y., Hwang, S., Sharma, M., Hagemann, H. and Akiba, E. Synthesis of a bimetallic dodecaborate $\text{LiNaB}_{12}\text{H}_{12}$ with outstanding superionic conductivity. *Chem. Mater.* 27, 5483 (2015).
- [56] Frisch M. J. et al., *Gaussian 03*, revision B.03; Gaussian, Inc.: Wallingford, CT, 2003.
- [57] Zhan, C., Nichols, J. A. and Dixon, D. A. Ionization potential, electron affinity, electronegativity, hardness, and electron excitation energy: Molecular properties from density functional theory orbital energies. *J. Phys. Chem.A* 107, 4184 (2003).
- [58] Blöchl, P. E. Projector augmented-wave method. *Phys. Rev. B* 50, 17953 (1994).
- [59] Perdew, J. P., Burke, K., Ernzerhof, M. Generalized gradient approximation made simple. *Phys. Rev. Lett.* 77, 3865 (1996).
- [60] Kresse, G. and Furthmüller, J. Efficiency of ab-initio total energy calculations for metals and semiconductors using a plane-wave basis set. *J. Comput. Mater.Sci.* 6, 15 (1996).
- [61] Kresse, G. and Furthmüller, J. Efficient iterative schemes for ab initio total-energy calculations using a plane-wave basis set. *Phys. Rev. B* 54, 11169 (1996).
- [62] Allen, M. P. and Tildesley, D. J. *Computer simulation of liquids*, Oxford university press: New York, 1991.
- [63] Grimme, S. Semiempirical GGA-type density functional constructed with a long-range dispersion correction. *J. Comput. Chem.* 27, 1787 (2006).
- [64] Heyd, J., Scuseria, G. E., Ernzerhof, M. Hybrid functionals based on a screened Coulomb potential. *J. Chem. Phys.* 118, 8207 (2003).
- [65] Chan, M. K. Y. and Ceder, G. Efficient band gap prediction for solids. *Phys. Rev. Lett.* 105, 196403 (2010).

- [66] Monkhorst, H. J. and Pack, J. D. Special points for Brillouin-zone integrations. Phys. Rev. B 13, 5188 (1976).